Hindawi Publishing Corporation
Advances in Condensed Matter Physics
Volume 2011, Article ID 867074, 14 pages
doi:10.1155/2011/867074

Research Article

Electronic Structure of the Cubic Compounds $ReGa_3$ (Re = Er, Tm, Yb, and Lu)

Helmut Bross

Arnold Sommerfeld Center, Ludwig Maximilians, University of Munich, 80333 Munich, Germany

Correspondence should be addressed to Helmut Bross, helmut.bross@physik.uni-muenchen.de

Received 28 September 2010; Revised 10 January 2011; Accepted 24 February 2011

Academic Editor: P. Guptasarma

The electronic structure of $ErGa_3$ and its isostructural compounds with Tm, Yb, and Lu are investigated with a highly accurate band structure scheme in LDA and GGA and warped muffin-tin approximation. In contrast to other investigations, the 4f electrons of the constituent Re are also treated as part of the valence bands. The position of the corresponding 4f bands relative to the Fermi energy E_F strongly depends on the nuclear charge of Re. In Lu, they lie almost by 0.5 Ryd below E_F and are extremely narrow. In Er, both in LDA and GGA, the 4f bands are found to be very close to the Fermi level E_F. Assuming most of the 4f electrons to be part of the core removes the disagreement almost completely but produces a Fermi surface with a topology markedly different from that proposed in previous investigations. The intersections of the Fermi surface with planes are strongly varying within the Brillouin zone, they do not well match with the sparse experimental results. Investigations using the LDA + U scheme as well as investigations of the dielectric response function are sketched.

1. Introduction

Studies on the electronic structure of cubic $ReGa_3$ (Re denotes the heavy earth metals Er, Tm, Yb, and Lu, resp.) compounds which crystallize in the $AuCu_3$ structure (see Figure 1) are a challenge not only as it is supposed that their magnetic properties are controlled by peculiarities of their Fermi surfaces but also as the role of the localized 4f electrons is not well understood.

In previous investigations of $ErGa_3$ and of $TmGa_3$ [1–6], which have been done to get detailed information about the shape of the Fermi surface, the 4f electrons are assumed to be part of the core contributing to the charge density without interacting with the other valence electrons. Using the linear muffin-tin orbital method (LMTO) in the atomic sphere approximation (ASA), Pluzhnikov et al. [2] and Petukhov et al. [3] found in the range of the high as well as the intermediate de Haas-van Alphen (dHvA) frequencies a quite good agreement between their ab initio calculations and the experimental data. In order to analyze measurements of the two-dimensional angular correlation of the annihilation radiation spectra [5] which give more details about the FS topology more modern schemes have been used: the full-potential LMTO and the full-potential linear augmented plane waves (FLAPW) schemes have been applied [6]. Disappointingly, none of these codes was able to produce a satisfying description of some experimental features that were in satisfying agreement with the previous LMTO-ASA results [2, 3]. It was supposed [6] that the most probable reason for this difference lies in the choice of the linearization energy E_l around which the expansion of the energy-dependent radial function $R_l(E, r)$ is performed, in LMTO as well as in FLAPW.

It is a question of principle importance whether the possible breakdown of the LDA in the cases of the compounds $ErGa_3$ and of $TmGa_3$ is a failure of the LDA scheme or if it is caused by fact that in these compounds the 4f bands fortuitously coincide with the Fermi level E_F and thus yield a density of states unrealistically enhanced at E_F. In the systematic analysis of the electronic structure of compounds consisting of rare earth metals neighboured in the periodic table done in present work, the second alternative turned out to be true.

The present investigations use the Modified Augmented Plane Wave (MAPW) method [7] scheme. It is a linearized version of Slater's APW method but differs from LAPW

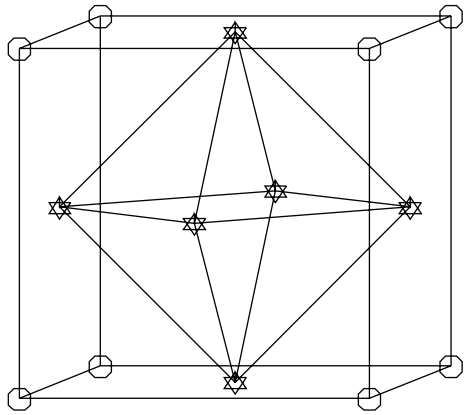

Figure 1: The fcc superlattice Cu_3Au. Open circles: Au, stars: Cu.

in that within the atomic spheres the radial part of the Bloch functions is a combination of radial functions $R_{s,l}$, counting the energies $E_{s,l}$ chosen within a broad range, which distinctly differ from each other. Thus, the above-mentioned problems of LAPW are avoided. In the context of the LDA DFT formalism, the MAPW scheme is almost free of any systematic restrictions and guarantees any desired accuracy by a suitable choice of the ansatz functions and of other intrinsic parameters.

This paper is organized as follows. Section 2 starts with a comparison of the essentials of the LAPW and the MAPW scheme. It is explained why the latter guarantees the high accuracy needed to properly describe the electronic structure of $ErGa_3$. The progress of self-consistent calculations incorporating many valence electrons, especially in the case of narrow 4f bands just below E_F, sensitively depends on the choice of the starting potential. Therefore, in Section 3, our study of the series of RE compounds were started with the compound $LuGa_3$ characterized by fully occupied 4f bands. Thus, we could avoid that the iteration mechanism stops at an incidental minimum. By reducing the Re core charge in noninteger steps, we could show how the 4f peak in the density of states curve approaches the Fermi level. This strategy actually makes self-consistent calculations faster and more stable because we remain near an absolute minimum in the high dimensional potential landscape. Then, the band structure, the shape of the Fermi surfaces including extremal areas, and cyclotron masses are discussed. In Section 4, investigations of the dielectric response function are sketched.

2. Basic Theoretical Aspects

2.1. Relativistic Effects. The heavy Re rare earth atom makes a relativistic treatment necessary. In previous investigations dealing with this aspect, the core and the valence electrons have been treated by completely different schemes. The atom-like core states were obtained by use of the four-component Dirac equation whereas the valence states were approximated by a two-component equation that has been derived, more or less, via successive applications of unitary, norm-conserving Foldy-Wouthuysen transformations. In the simplest case, the so-called scalar relativistic approach, a modified Pauli or radial Schrödinger equation containing the relativistic mass correction and the Darwin term, is solved within the spherical regions [2, 4]. More refined investigations [5, 6] make the expectation value of a Hamiltonian containing the spin-orbit coupling stationary, with a Ritz ansatz obtained in the scalar-relativistic approximation. It is obvious that the orthogonality of the core states to the valence states is destroyed by the use of completely different Hamiltonians. Test calculations on Au [8] that go beyond the approximations just described (because they are based on nonrestricted two-component spinors) yielded the result that this improper treatment of the relativistic effects produces uncontrolled errors in the charge density and the total energy. Therefore, as long as a fully relativistic treatment of compounds similar to the treatment of solids containing only one atom in the cell [9] is outstanding, a nonrelativistic is regarded as more reliable.

2.2. LAPW versus MAPW: A Critical Comparison. It is common to both the LAPW and the MAPW [7] methods that the Bloch functions $\langle \vec{r} \mid n\vec{k} \rangle$ outside the APW-spheres are approximated by superpositions of plane waves, and that within the APW spheres, the plane waves are suitably augmented, yielding a linear eigenvalue problem. This has been done in different ways. In LAPW, the wave function consists of a sum of products of a spherical harmonic Y_{lm} and a linear combination of two radial functions. The first is a solution of the radial differential equation inside the atomic sphere with an averaged spherical potential and a linearization energy $\mathcal{E}_l$, around which the expansion of the energy dependent wave functions is performed. The second one is the energy derivative of the radial function. Up to the maximal value of the angular momentum $\mathcal{L}_{\max}$, the linear combination at the surface of the APW-sphere, joins continuously to the angular momentum expansion of the corresponding plane wave. As for all $l > \mathcal{L}_{\max}$, no continuity exists, and the truncation error can be made small by choosing, large $\mathcal{L}_{\max}$, for example, 10. As a consequence of this choice of the radial functions, the solutions of the eigenvalue problem are most reliable at energies around $\mathcal{E}_l$. The range of validity around $\mathcal{E}_l$ can be quite small when the branches of the logarithmic derivatives $R'(r_{\mathrm{APW}})/R(r_{\mathrm{APW}})$ follow in rapid succession as is the case in $ErGa_3$. Because the sets of eigenfunctions obtained with different values of $\mathcal{E}_l$ are not strictly orthogonal to each other, a change of the relevant energy $\mathcal{E}_l$ is not a good remedy.

In the MAPW scheme, a set of radial functions R_{sl} is generated in the spherical averaged potential, mostly by requiring that their logarithmic derivative is either $+1$ or -1. To avoid any truncation error, the augmentation of the plane waves is only performed for the leading angular numbers $l \leq l_{\max}$, whereas for $l > l_{\max}$, the spherical Bessel functions j_l are kept. In contrast to all other versions of the APW scheme, the full wave function and its derivative are made exactly continuous on the surface of the APW spheres by

the use of additional constraints. To account for the special role of the 4f electrons, the basis of the radial functions within the Re spheres contains one radial function that is optimally localized by an appropriate choice of the radial energy, implying that the value of the radial wave function on the APW sphere is smaller by almost a factor of 100 than the others. Further 4f radial functions are chosen according to the previously mentioned recipe, guaranteeing the continuity of the the corresponding partial wave.

2.3. Details of the MAPW Calculation. The following considerations are based on the assumption that the Re core has a Pd-type configuration consisting of 46 electrons. We have found that the states up to 4d are welllocalized; for example, their radial functions assume values less then $0.6 \cdot 10^{-3}$ on the surface of the Er sphere, and need not to be considered in the MAPW calculations. Nevertheless, they are numerically orthogonal to the wave functions of the valence states because they are not kept frozen during the self-consistency cycles. In contrast, the best localized 4f state of Er assumes the value 0.032413 a.u. on the Er sphere confirming our reservation against treating this state as part of the core.

The quantum number l of the angular decomposition of the Bloch functions is restricted to be less than or equal to 2 within the Ga spheres and to be less than or equal to 3 within the Re spheres. Four radial functions $R_{sl}(r)$ are used for each of the $l \leq 3$. The proper choice of the 4f radial functions needs special care as the corresponding logarithmic derivative is strongly varying in the energy region near the Fermi level.

The number of plane waves used to describe a Bloch state $|\vec{k}\rangle$ within the whole atomic polyhedron is restricted by the inequality

$$\left(\vec{k}+\vec{K}\right)^2 \leq 12\left(\frac{2\pi}{a}\right)^2, \tag{1}$$

where $\vec{K}$ denotes the vector of a simple cubic reciprocal lattice, and a is the lattice constant. In contrast to the plane-wave cutoff mostly applied in LAPW it guarantees the full point symmetry of the Bloch energies at any point of the Brillouin zone (BZ). Depending on the specific value of the wave vector $\vec{k}$, this restriction yields a superposition consisting of between 160 and 181 plane waves. In total, each ansatz consists of more than 320 trial functions. It guarantees sufficient accuracy of the Fermi energy and of the total energy in the SCF cycles and leaves the topology of the band structure almost stationary, that is, no jumps are visible in the intersection of the Fermi surface with certain planes, as shown in Figures 7, 8, 9, 10, and 12.

The Brillouin zone integrations over all occupied states yielding the electron density ρ, the Fermi energy E_F, and the total energy E_{tot} are approximated by a sum over MG^3 points of a simple cubic lattice of length $(1/MG)(2\pi/a)$ within one octant of the BZ. Because the evaluation of ρ requires those operations of the subgroup of the point group Q_h that leave the atoms of the basis invariant, a further restriction to the irreducible wedge of the fcc BZ is not possible, at least in the SCF cycles.

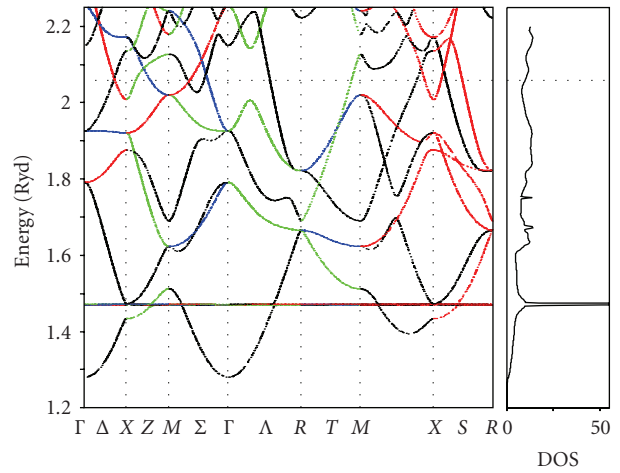

FIGURE 2: Left panel: Band structure of $LuGa_3$ with lattice constant $a = 4.212$ Å. $E_F = 2.059387$ Ryd. The horizontal line at 1.4712 Ryd denotes the 4f bands. Black line: $\Delta_1, Z_1, \Sigma_1, \Lambda_1, T_1$ representations, red line: $\Delta_2, .2, \Sigma_2, \Lambda_2, T_2$ representations, green line: $\Delta_2', Z_3, \Sigma_3, \Lambda_3, T_2'$ representations, blue line: $\Delta_5, Z_4, \Sigma_4, T_5$ representations. Right panel: density of states in units of electrons $\text{cell}^{(-1)}$ $\text{Ryd}^{(-1)}$, dashed line denotes the position of the Fermi level. Figure 3 illustrates the position of the symmetry points and of the lines within the BZ.

The characteristic ground-state properties are calculated by use of elaborate exchange-correlation functionals in LDA [10] and GGA [11–14]. Without any further truncation, exchange and correlation within the atomic spheres are obtained from the charge density along the special directions. Outside the spheres, the charge density is evaluated on a fine mesh of suitably chosen $\vec{r}$-points [15] which allows to determine exchange and correlation in any accuracy wanted. Further details of the present calculation are described in previous publications [16, 17].

3. Results

3.1. Trends in the Electronic Structure of the Isostructural Compounds $ErGa_3$, $TmGa_3$, $YbGa_3$, and $LuGa_3$ in LDA. The following investigations aim to provide an overall insight into the influence of the 4f electrons. To avoid any influence of the lattice spacing, all investigations have been done with the lattice constant of $ErGa_3$ at zero temperature, $a = 4.212$ Å [4]. The narrow Re-5s and 5p bands with energies around -0.5764 Ryd and 0.7636 Ryd, respectively, in the case of $ErGa_3$ are well separated from the complex of the other bands originating from the atomic Re 6s- and 5d-states and are not to be considered.

In the course of these considerations, we have found that the electronic structure of the compound $LuGa_3$ is standing out for its relative simplicity. As shown in Figure 2, the 4f electrons occupy a band of extremely small width of 3 mRyd located by more than half of a Rydberg below the Fermi level. It is split according to the cubic symmetry and additionally hybridized with the single band starting at the lowest Γ state.

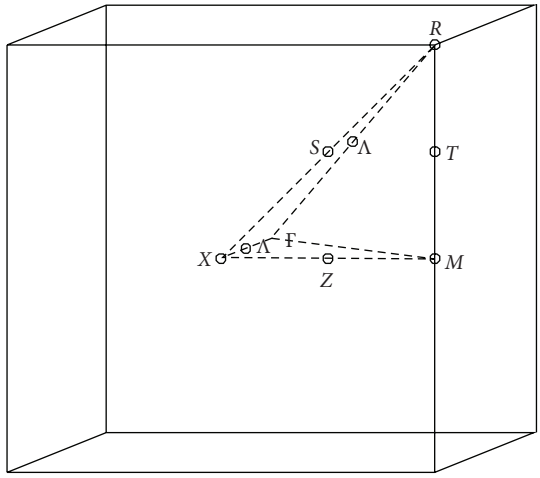

FIGURE 3: Brillouin zone for the simple cubic Bravais lattice. The notation of the symmetry points and lines follows [18].

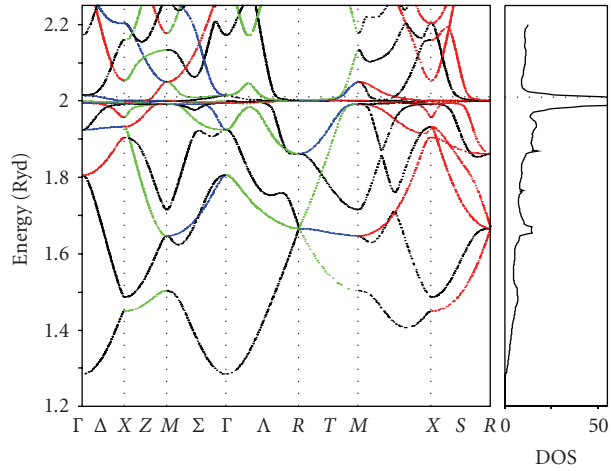

FIGURE 5: Band structure and density of states of $TmGa_3$ with lattice constant $a = 4.196$ Å [2] and $E_F = 2.009753$ Ryd. For further details see Figure 2.

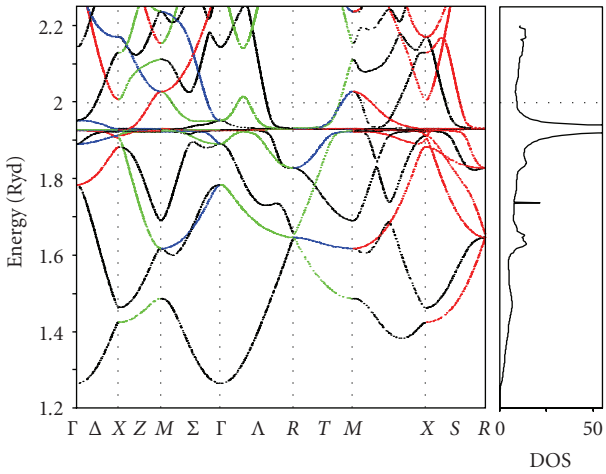

FIGURE 4: Band structure and density of states of $YbGa_3$ with lattice constant $a = 4.212$ Å and $E_F = 1.999407$ Ryd. For further details, see Figure 2.

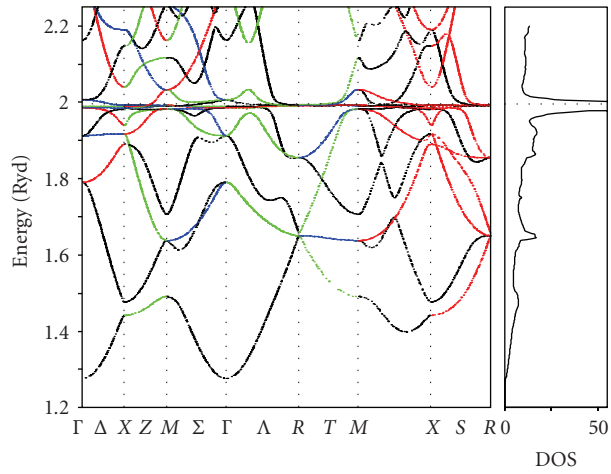

FIGURE 6: Band structure and density of states of $TmGa_3$ with lattice constant $a = 4.212$ Å [2] and $E_F = 1.996388$ Ryd. For further details see Figure 2.

It is remarkable that it leaves the other bands almost unchanged with the favourable effect on the self-consistency that a small number of cycles is sufficient. Thus, the final potential is best suited as a reliable starting point for the investigations of the other isostructural compounds.

Table 1 lists some characteristic quantities found by successive decrease of the nuclear charge of the Re constituent, Z_{nuc}, in noninteger steps, starting from the last line. It causes the energy of the best localized 4f radial state, $E_{1,3}$, continuously to rise whereas the Fermi energy slightly diminishes. Both energies get closer and closer but do not cross. This change is accompanied by a strong increase of the hybridization of the 4f states with the other valence bands, although the wave function of the best localized 4f radial state at the APW sphere only moderately increases from 0.0208 a.u. to 0.0323 a.u. in $ErGa_3$. Correspondingly, $N(E_F)$ raises but does not tend to the unphysical values cited in [2]. There is no doubt that in the cases of $TmGa_3$ and $ErGa_3$ the corresponding values are still too large compared with experimental results. Figures 4, 5, and 6 illustrate how the Re nuclear charge influences the band structure along the lines of high symmetry in the Brillouin zone. In their overall look, all Figures are rather similar; however, significant differences are visible in the range of the 4f bands and their location relative to the Fermi level.

To emphasize the role of the Re 4f bands as possible sinks of electrons, we have calculated the f orbital projected density. The number of f-electrons per rare-earth atom, $Z_{4f}(E_F)$, listed in Table 1 in the last but one column, increases up to $Z_{\text{nuc}} \approx 70.1$ almost in the same measure as the virtual core charge and reversely the Fermi energy decreases. Above this value, all 4f-like states are occupied and the additional

Table 1: Energy $E_{1,3}$ of the best localized 4f radial state, Fermi energy E_F, density of states at the Fermi level $N(E_F)$, f resolved density of states $N_{4f}(E_F)$, and number of 4f electrons $Z_{4f}(E_F)$ per Re atom. Last column: value of the best localized 4f radial state at the APW sphere. Energies in Ryd and densities of states in electrons cell $^{-1}$ Ryd $^{-1}$.

Z_{nuc}	$E_{1,3}$	E_F	$N(E_F)$	$N_{4f}(E_F)$	$Z_{4f}(E_F)$	
68.00	1.99673	1.99917	178.51055	163.28079	11.7888	0.032286
68.25	1.99337	1.99530	144.41692	129.80704	12.0677	0.032002
68.50	1.99215	1.99530	116.63079	102.57300	12.2938	0.031850
68.75	1.98843	1.99288	89.01376	75.98205	12.5443	0.031450
69.00	1.98413	1.99052	58.31993	46.82609	12.7942	0.031069
69.25	1.97924	1.98868	40.87829	30.40385	13.0363	0.030684
69.50	1.97191	1.98682	24.92342	16.16095	13.2867	0.030259
69.75	1.96031	1.98813	11.39923	4.77653	13.5222	0.029762
70.0	1.93251	1.99847	7.64239	1.04675	13.7220	0.028962
70.3	1.84650	2.01689	8.03116	0.20343	13.8744	0.027075
70.5	1.75745	2.02962	8.82774	0.13170	13.9296	0.025372
70.7	1.65198	2.04194	9.27159	0.11006	13.9608	0.023550
71.0	1.47513	2.05984	9.86605	0.11126	13.9885	0.020820

electrons occupy the s-p-d like states which are less and less hybridized with the 4f states. The Fermi energy starts to rise and $N(E_F)$ approaches moderate values. This change occurs at a noninteger value of Z_{nuc}: the compound $YbGa_3$ stands on one side and the compound $LuGa_3$ on the other, and consequently their crystal potentials are significantly different. According to Table 1, the projected 4f density $N_{4f}(E_F)$ substantially contributes to the large value of $N(E_F)$ especially in the case of $ErGa_3$ and $TmGa_3$.

These considerations are further illustrated by the plots of the density of states (DOS) displayed in the right panels, respectively. The sharp peak caused by the 4f band approaches the Fermi level with decreasing values of Z_{nuc}. In $ErGa_3$, the energy distance amounts up to 4 mRyd. The non-4f part of the DOS is rather similar in the four compounds and is quite smooth. From these results, we learn that the large value of $N(E_F)$, especially in the case of $ErGa_3$, in contradiction to experimental facts is not a systematic deficit of LDA, but it is almost accidental as it locates the position of the 4f bands near to the Fermi level. Only a small shift of the position of the 4f bands by about 5 mRyd will improve the agreement with the experimental data considerably. On the other hand, these results do not support at all the concept of assuming 11 or 12 electrons as part of the core [2, 4].

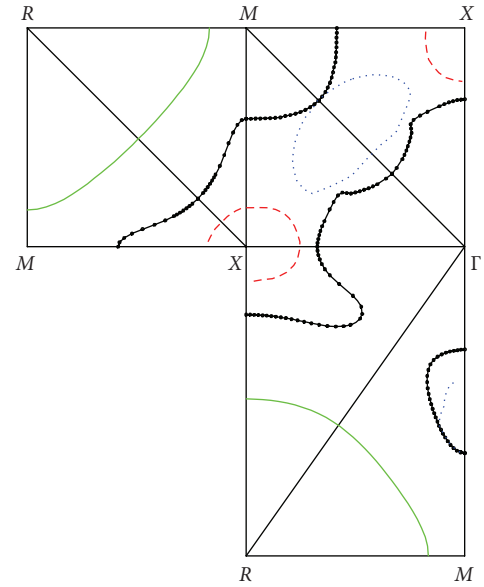

Figure 7: Intersection of the Fermi surface of $LuGa_3$ with high symmetry planes. The various sheets are marked by different colours.

3.2. Fermi Surface in Strict LDA and GGA. It is evident that the position of the 4f bands relative to the Fermi level has significant influence on the shape of the Fermi surface. To tie on to previous investigations [2, 4–6], we first consider intersections of the Fermi surface with high symmetry planes, the panels ΓXMX, RMXM, and ΓXRM.

In the case of $LuGa_3$, displayed in Figure 7, we find a certain resemblance to the FLAPW results derived for $ErGa_3$ [6], especially in the lower panel showing the intersection with the (011) plane. The intersection with the plane $k_z = 0$ displayed in the upper panel is a bounded contour of almost elliptic shape whereas in FLAPW the central contour merges with the contours encircling the occupied states around the X-points. The LMTO-ASA results of $ErGa_3$ discloses a minor similarity as the contours of the occupied states around the M points extend far in the direction of the Γ point. In $YbGa_3$, the intersections look quite similar.

The contour lines of $ErGa_3$ shown in Figure 8 disclose a completely different shape of the Fermi surface. This already follows from the band structure displayed in Figure 6 which shows that twofold degenerated sheets of the Fermi surface cross the Δ- and the T-lines producing cusps on the

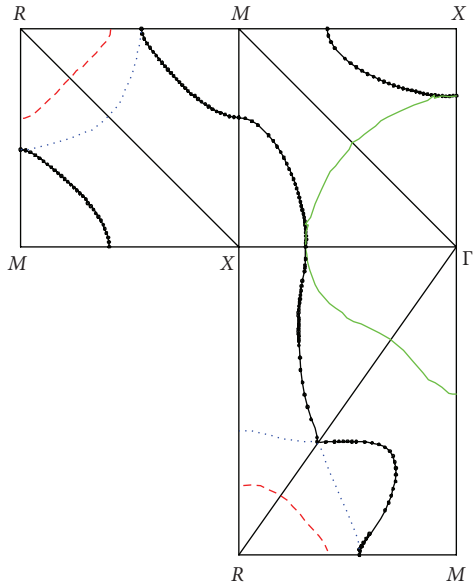

FIGURE 8: Intersection of the Fermi surface of $ErGa_3$ with high symmetry planes. $E_F = 1.996388$ Ryd. Solid line (green): b_1, broken line (red): b_2, dotted line (blue): b_3, and points connected by a thin line: b_4. The Fermi sheets b_1, b_2, b_3, and b_4 are described in the text.

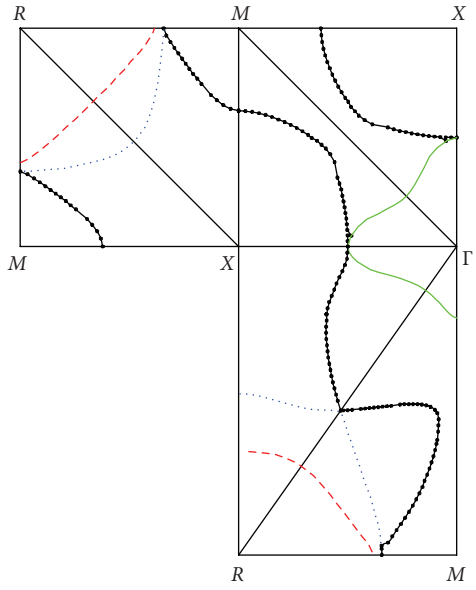

FIGURE 9: Intersection of the Fermi surface of $TmGa_3$ with high symmetry planes. $E_F = 2.009753$ Ryd. For further details, see Figure 8.

respective boundary lines. Contours around the M- and R-points encircle occupied states whereas the surrounding of the Γ- and X-points are not occupied. The lines encircling the points M, R, and X are the tracks of electron sheets, whereas the line around Γ is the track of a hole sheet. It is remarkable that the intersections of the Fermi surface for $TmGa_3$, displayed in Figure 9, are quite similar to that of $ErGa_3$ although their densities of states differ by more than a factor 3.

An extensive analysis in 3 dimensions which is straightforward but quite arduous had the result that the Fermi surface of $ErGa_3$ consists of four sheets: three, more or less, spherically shaped surfaces denoted by b_1, b_2, and b_3 all having the full cubic point symmetry O_h. The hole FS b_1 is centered at the Γ point whereas the electron surfaces b_2 and b_3 are located at the R point. Finally, the FS b_4 is multiply-connected and extends over the whole BZ and is best described by its intersections with planes $k_3 = \text{const.}$ displayed in Figure 10 in steps of $\Delta k_3 = 0.25 \cdot 2/a$. For completeness, the cross-sections with other surfaces are also shown. From this Figure, we learn that the FSs b_1, b_2, and b_3 are monotonically shrinking with increasing value of k_3, indicating that the cross-sections are extremal at the surface of the first BZ. According to Figure 10, the FS b_1 is strongly indented in the (111) direction. The FS b_4 continuously changes its shape. Up to $k_3 \approx 0.125 \cdot 2\pi/a$ it is outside of the cylinder around $(0, 0.5, k_3)$, then rapid changes of its shape occur and beyond $k_3 = 0.375 \cdot 2\pi/a$, it is again outside of the cylinder around $(0, 0.5, k_3)$. It is evident that the intersections with planes oriented in (110) and (111) with the FS b_4 also reflect this great variety of orbits. The investigations in Section 3.3 will have similar results. Intersections of the type b_1, b_2, or b_3 which are easy to comprehend, and those of type b_4 which show a great diversity of intersections. These findings distinctly demonstrate that the customary plots [2, 4–6] of the panels ΓXMX, RMXM and ΓXRM do not capture the great variety of orbits which change rapidly mostly inside the Brillouin zone. Our results also cast doubts on the methods usually applied to reconstruct the Fermi surfaces of such compounds like $ErGa_3$ directly from experiments (de Haas-van Alphen, cyclotron resonance, electron-positron annihilation measurements) which are mostly based on the assumption that the FS has some well-defined cross-sections [19].

The GGA using the functionals [11–14] almost rigidly shifts the band structure of $ErGa_3$ to lower energies by 50.0 mRyd but has only minor influence on the shape of the Fermi surface. The energy of the best-localized 4f radial states $E_{1,l=3}$ is even closer to the Fermi energy than in LDA, that is, 1.8 mRyd, with the fatal consequence that the density of states at the Fermi level assumes the unphysical value of 195.2 electrons cell^{-1} Ryd^{-1}. Consequently, sections of the Fermi surface with the high symmetry planes of the Brillouin zone look quite similar to those displayed in Figure 8. Hence, GGA does not improve agreement with the experimental data at all.

3.3. Exclusion of the Hybridization of the Valence Bands by the 4f Electrons: Following Previous Tracks. Our investigations have the result that, based on experimental evidence [4, 6], the three-dimensional mapping of the Fermi surface of $ErGa_3$ could not be explained by high-accurate LDA-MAPW calculations if the 4f-electrons are considered to be constituents of the valence bands. The strong influence of the 4f bands on the topology of the Fermi surface of $ErGa_3$ and $TmGa_3$ is avoided by treating them as part of the core as has been done in previous investigations [2, 4–6]. Then, in the MAPW scheme, the quantum number l

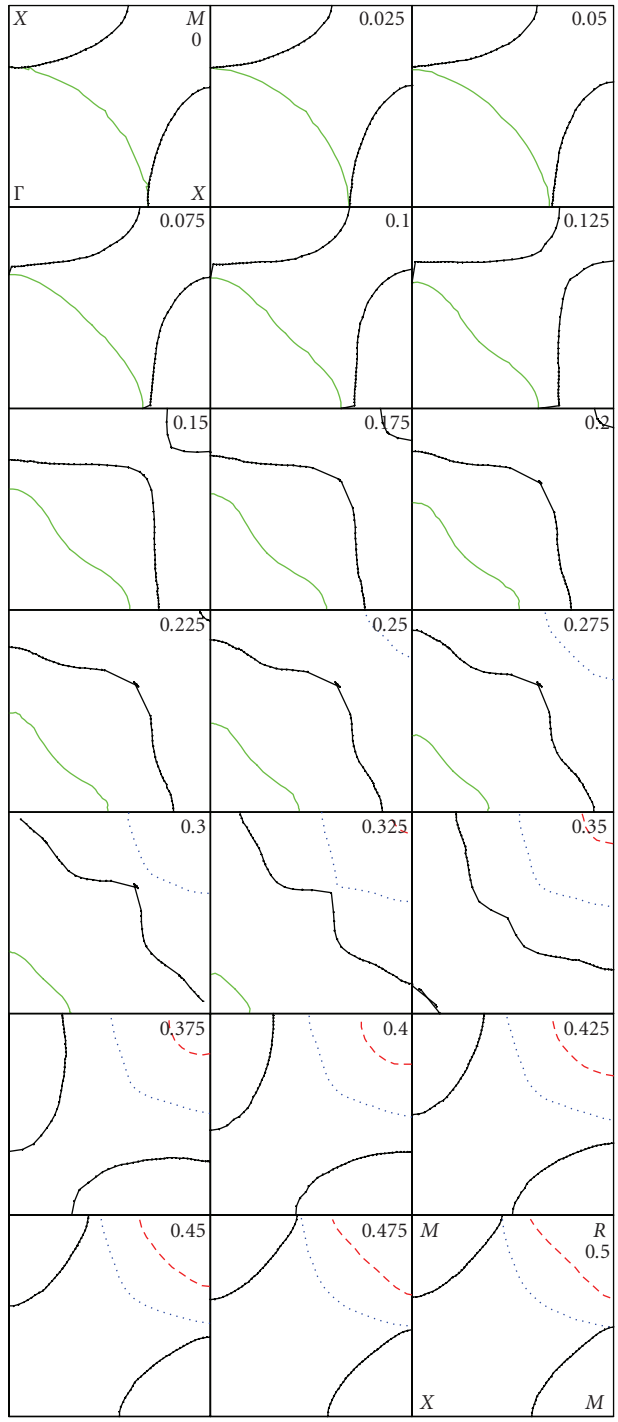

Figure 10: Intersections of the Fermi surface of $ErGa_3$ with planes $k_3 = \text{const}$. Each square is bounded by the lines $k_1 = 0$, $k_1 = \pi/a$, $k_2 = 0$, and $k_2 = \pi/a$. The actual value of k_3 is given in the upper right corner. Solid line (green) b_1, broken line (red) b_2, dotted line (blue) b_3, and points connected by solid line (black) b_4. By virtually placing these squares in stacks one over the other, an insight into the various FSs is obtained.

of the angular decomposition of the Bloch functions may also be restricted to be less than or equal 2 within the Er or Tm spheres. Self-consistent calculations yielded the result that the energy of the 4f-orbitals is below the Fermi level by half a Rydberg in the case of the Er $4f^{11}$ core whereas it is distinctly above the Fermi level when an additional 4f electron is assumed as belonging to the core. The band structure of the Er $4f^{11}$ configuration, displayed in Figure 11, as well as that of the Tm $4f^{12}$ configuration shows a great similarity with that of the $LuGa_3$, but they differ markedly

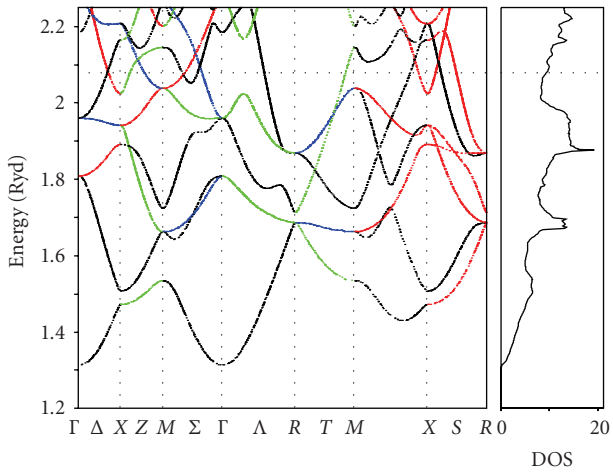

FIGURE 11: Band structure and density of states of $ErGa_3$ for the $4f^{11}$ configuration with lattice constant $a = 4.212$ Å [2] and $E_F = 2.078341$ Ryd. For further details, see Figure 2.

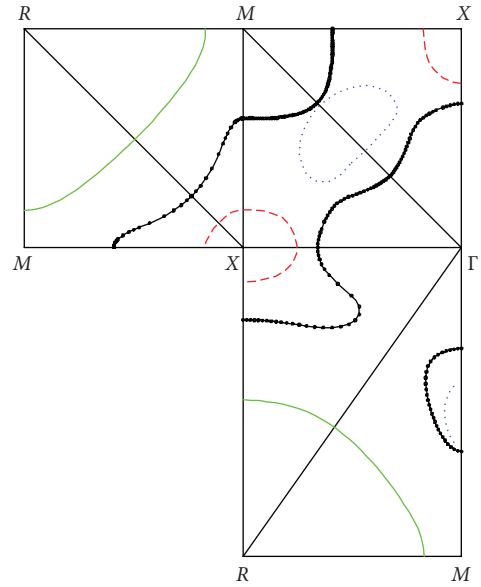

FIGURE 12: Intersection of the Fermi surface of $ErGa_3$ with high symmetry planes derived for the Er $4f^{11}$ core configuration. $E_F = 2.078341$ Ryd. Full line (green): B_1, broken line (red): B_2, dotted line (blue): B_3, and points connected by a thin line: B_4. Note the close similarity with the case of $LuGa_3$ displayed in Figure 5.

from the band structure found when the 4f electrons are assumed to be part of the valence electrons (see Figure 6). Consequently, the Fermi topology is completely changed. This is illustrated in Figure 12, showing the contour lines of the Fermi surface. Compared with FLAPW results obtained with the same concept [6], the sections with the (110) plane displayed in the XMRM face are quite similar, but some sections with the (100) plane are completely different. A coarse resemblance to the LMTO-ASA [4] result also exists. In contrast, the contour plots of the Er $4f^{12}$, not shown here, disclose a completely different Fermi surface topology for which we have no experimental evidence. The plot of the density of states $N(E)$ displayed in the right panel of Figure 11 shows some van-Hove singularities with modest heights.

The values of $N(E_F)$ are in a reasonable range, for example, 10.34 and 9.60 electrons cell^{-1} Ryd^{-1} in the Er $4f^{11}$ and the Tm $4f^{12}$ configurations, respectively, and are even smaller by 30% if the number of the 4f electrons in the core is increased by one. From these results, we learn that within a heuristic approach, we could achieve closer agreement with the low temperature specific heat data by choosing the nonintegral parameter x of the Er $4f^x$ core configuration to be near the value 11.0.

The Fermi surface in the Er $4f^{11}$ core configuration consists of four sheets: B_1 is almost spherical in shape around the point R, slightly dented in (011), with a mean radius $0.3826 \cdot 2\pi/a$. B_2 is a prolate spheroid around the point $X(0,0,0.5)$ with the longest axis in the (001) direction. The lengths of its axis are approximately $0.1441 \cdot 2\pi/a$ and $0.0868 \cdot 2\pi/a$. B_3 is almost ellipsoidally shaped around the point $(0.2730,0.2730,0)\ 2\pi/a$ with the longest axis oriented in (110) directions. The lengths of its axes are approximately $0.1356 \cdot 2\pi/a$, $0.0721 \cdot 2\pi/a$, and $0.0387 \cdot 2\pi/a$. Finally, B_4 is multiply-connected and again is best described by its intersections with planes $k_3 = \text{const}$, as displayed in Figure 13 together with those of the other Fermi surfaces. Similar to the FS b_4 shown in Figure 10, its shape exhibits rapid variations within the BZ.

According to Figure 12, besides the contours of B_2 and B_3, two contours of B_4 exist near the face ΓXMX. One is almost circular the centre being over the point M whereas the other has fourfold symmetry around the point Γ. With increasing value of the component k_3, the contours of B_2 and B_3 shrink whereas those of B_4 grow, merge for $k_3 = 0.0823 \cdot 2\pi/a$, and then split into two other parts with contours centred above X points. Being well separated in the range $0.1 \cdot 2\pi/a \le k_3 \le 0.225 \cdot 2\pi/a$, both curves merge again at $k_3 = 0.28 \cdot 2\pi/a$ and form considerably larger contours centred below the R point for $0.228 \cdot 2\pi/a \le k_3 \le 0.280 \cdot 2\pi/a$. For still larger values of k_3, the size of the contours, again centred around the Γ X line gradually shrinks. The intersections of the sheet B_4 with planes normal to the (110) and (111) directions even show a still greater diversity. Besides closed contours, now in certain ranges of the projection of $\vec{k}$ on the normal direction, contours exist that extend over the whole reciprocal lattice space, yielding the so-called open orbits. In general, the shape of the contours shows rapid changes, especially near $0.3 \cdot 2\pi/a$.

It is surprising that even in the present case, considering the 4f electrons as part of the core possible cross-sections of FS can rapidly change inside the BZ, and they are not at all described by the usual plot of the contour line only showing the faces ΓXMX, $RMXM$, and ΓXRM. We suspect that a thorough analysis using the LAPW scheme will produce a similar behaviour provided the plane waves satisfy a criterion analogous to that quoted in Section 2.3.

3.4. Extremal Areas and Cyclotron Masses of $ErGa_3$. The extremal cross-sectional areas and the corresponding cyclotron masses for the closed Fermi sheets are listed in

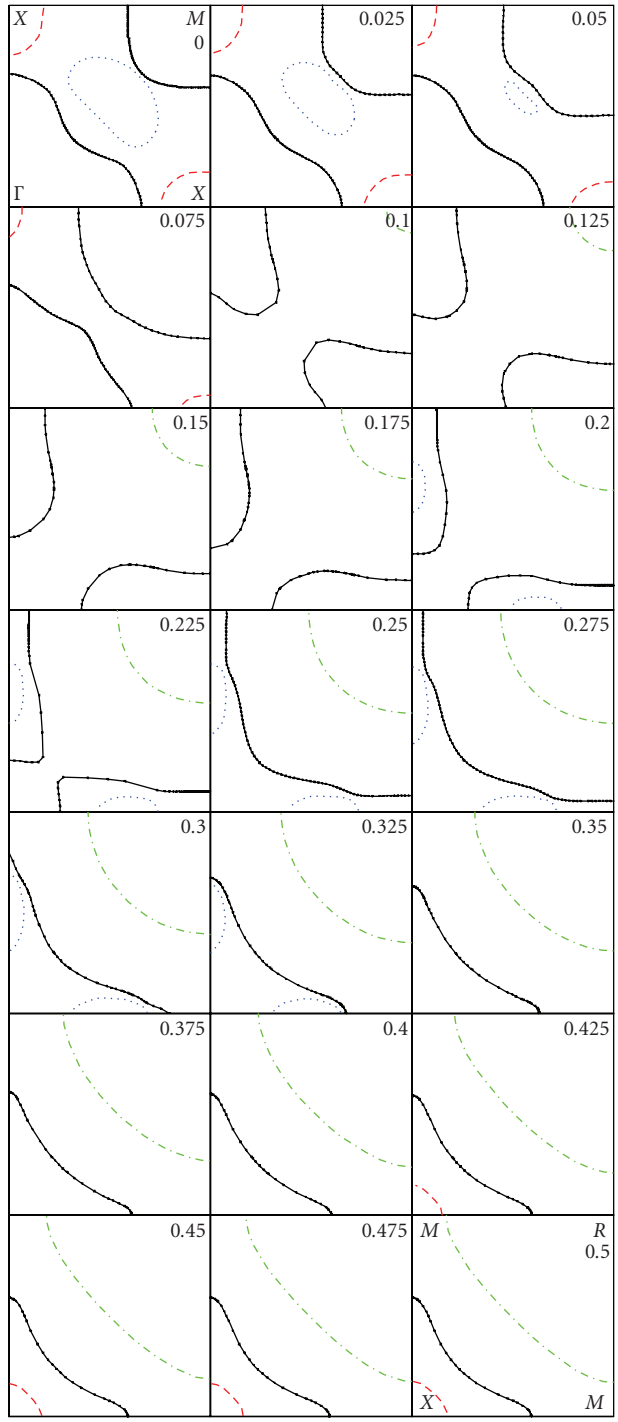

FIGURE 13: Intersection of the Fermi surface of $ErGa_3$ with planes k_3 = const derived for the Er $4f^{11}$ core configuration. Each square is bounded by the line $k_1 = 0$, $k_1 = \pi/a$, $k_2 = 0$, $k_2 = \pi/a$. The actual value of k_3 is given in the upper right corner. Full line (green): B_1, broken line (red): B_2, dotted line (blue): B_3, and points connected by a thin line: b_4.

Table 2 (the areas $\mathcal{A}$ of the cross-sections are related to the magnetic field B, in gauss, by the relation $(a/2\pi)^2\mathcal{A} = 4.2897\ 10^{-9}$ B in the case of the lattice constant cited by Pluzhnikov et al. [4]). Because of their spherical shapes, the areas of the Fermi sheet b_1 are slightly orientationally dependent, within a margin of 10%. Both FS b_2 and b_3 have, as a consequence of their dimension, such small areas that they need no further consideration. As a consequence of the strong change of the shape of the FS within the BZ, the areas and the cyclotron masses of b_4 listed in Table 3 cover a wide spectrum of values strongly depending on the vector pointing to the centre of the corresponding contour. It is questionable whether the usual

Table 2: Extremal cross-sectional areas $\mathcal{A}$ and the corresponding cyclotron masses m_c of the sheets b_1, b_2, and b_3 of $ErGa_3$. $\mathcal{A}$ in units of $(2\pi/a)^2$. m_c in units of the free electron mass.

FS	(001)		(110)		(111)	
	$\mathcal{A}$	m_c	$\mathcal{A}$	m_c	$\mathcal{A}$	m_c
b_1	0.4598	0.6136	0.4366	0.5579	0.4114	0.5602
b_2	0.0214	0.1869	0.0319	0.2372	0.0284	0.2604
b_2	0.0355	0.3290	0.0262	0.2375	0.0284	0.2600
b_3	0.0311	0.5333	0.0166	0.2294	0.0193	0.2757
b_3	0.0117	0.2114	0.0159	0.3039	0.0107	0.1872
b_3			0.0088	0.1321		

Table 3: Cross sectional areas $\mathcal{A}$ and the corresponding cyclotron masses m_c of the sheets b_4. Same units as in Table 2.

(001)		(110)		(111)	
$\mathcal{A}$	m_c	$\mathcal{A}$	m_c	$\mathcal{A}$	m_c
(0.101,0.357)	(0.442,1.631)	(0.155,0.216)	(0.478,0.859)	(0.031,0.182)	(0.380,1.251)
(0.748,0.766)	(1.453,1.607)	(0.296,0.376)	(0.265,0.369)	(0.574,0.714)	(0.927,1.275)

approach which simply connects the de Haas-van Alphen frequencies with extremal areas of the FS, is applicable [19] when the cross-sections show the strong variations found in the previous sections.

The Fermi surface and the cyclotron masses of $ErGa_3$ were investigated by Pluzhnikov et al. [4] by de Haas-van Alphen measurements in sufficiently strong magnetic fields destroying the antiferromagnetic phase. They found that the measured dHvA frequencies arranged in four branches that are orientationally independent to within a margin of at most 2%. The highest branch denoted by *a* can be uniquely attributed to the FS b_1; the measured values 0.4211, 0.4100, and 0,4210, in units of $(2\pi/a)^2$ in (001), (110), and (111), respectively, agree satisfactorily with the corresponding values in Table 2. The following two branches, denoted by *b, d,* and d', are due to the FS b_4. However, the values listed in Table 3 cover a far broader range than the experimental values, all in the same units, 0.1763, 0.1298, 0.0519 in (001)-, 0.0678, 0.0649, 0.0513 in (110)-, and 0.1522 in the (111)-direction, and are far more orientationally independent. Finally, the FS b_2, b_3, and some of the contour lines of b_4 produce the low-frequency branch, *h*. The good agreement between the experimental data with the ab initio calculations (carried out using the linear muffin-tin orbital method in the atomic sphere approximation with the 4f Er electrons as part of the core) performed by Pluzhnikov et al. [4] seems to be rather fortuitous in the light of our more accurate investigations, according to which only the orbit around R is expected to be orientationally independent and is characterized by a high dHvA frequency. Finally, the large discrepancies between the measured and theoretical values of the cyclotron masses found in both investigations can hardly be explained by many-body enhancement, as has been done by the previous authors [4], but raises the suspicion that the high magnetic fields applied to destroy the antiferromagnetic phase of $ErGa_3$ have a nonnegligible influence on the electronic structure.

3.5. LDA + U Investigations [20]. A simple way to describe the correlation between the localized 4f-Er electrons beyond the usual LDA is provided by the so-called "LDA + U" total-energy functional [21–23]. We have found that the MAPW scheme is especially suited for the implementation of this functional. Due to the lack of detailed information about the screened interaction, we assumed that the effective on-site Coulomb interaction has the form of a screened Coulomb potential with the screening length q as a free parameter. As desired, the reasonable value of $q = 3.0\,\text{Bohr}^{-1}$ shifts the narrow 4f bands by ≈0.3 Ry below the Fermi level and leaves the other bands almost unchanged with the consequence that $N(E_F)$ is found to be in quite good agreement with the experimental data. Details concerning the band structure are described in [20] giving evidence that the band structure is quite similar to those in LDA displayed in Figure 6 apart form the line MX. But it shows no similarity at all with the frozen core results described in Section 3.3.

4. A Sketch of the Investigations of the Dielectric Response

The response to a scalar electric field is fully described in the framework of the time-dependent density-functional theory by the the Kohn-Sham response function χ [24–27]. In the case of a slowly varying perturbation, it uniquely splits into an intraband and interband contribution. The first can be expressed by a sum over the Fermi surface,

$$\chi_{\text{intra}}(0,0,\omega) = -\frac{q_\mu q_\nu}{\hbar^2\omega^2} 2\sum_{n,\vec{k}} \frac{\partial\epsilon_{n,\vec{k}}}{\partial k_\mu}\frac{\partial\epsilon_{n,\vec{k}}}{\partial k_\nu}\frac{\partial f\left(\epsilon_{n,\vec{k}}\right)}{\partial\epsilon_{n,\vec{k}}}. \quad (2)$$

Table 4: Density of electrons, inverse band mass, mean value of the inner product grad$\epsilon_{n\vec{k}} \cdot$ grad$\epsilon_{n\vec{k}}$, band plasma frequency $\omega_{pl,b}$, free plasma frequency $\omega_{pl,f}$, and the ratio of the compounds' static conductivities to the conductivity of Cu at room temperature. All in atomic units.

Cu	0.23481	.074400	1.07386	0.6677	3.4617	1.0
Er	0.06148	0.01096	0.00290	0.1301	1.7579	0.00270
Tm	0.06419	0.02502	0.02131	0.2008	1.7962	0.01985
Yb	0.06544	0.12338	0.7997	0.4505	1.8137	0.74484
Lu	0.06743	0.16256	0.6861	0.5249	1.8410	0.63904

Einstein summation convention over μ and $\nu \in 1, 2, 3$. This relation is physically interesting: the mean value of the inner product of the velocities of the Bloch electrons at the Fermi surface essentially determine the dc behaviour. A highly simplified treatment of the dc-conductivity based on the assumption of a relaxation time τ describing the scattering of the electrons by lattice defects or phonons has the result

$$\sigma_{\mu\nu}(0) = -\frac{e^2}{\hbar^2 V_c} 2 \sum_{n\vec{k}} \tau\left(\epsilon_{n,\vec{k}}\right) \frac{\partial \epsilon_{n,\vec{k}}}{\partial k_\mu} \frac{\partial \epsilon_{n,\vec{k}}}{\partial k_\nu} \frac{\partial f}{\partial \epsilon_{n,\vec{k}}}, \tag{3}$$

V_c volume of the elementary cell. This expression is based on more general assumptions than those leading to the well-known Drude formula: (i) the solution of the Boltzmann equation by a $\vec{k}$-dependent relaxation time and (ii) Kohler's variational principle [28, 29] using the trial function grad $\epsilon_{n,\vec{k}}$.

Provided the relaxation τ can be assumed to be constant the cofactor of ω^{-2} in (2) gives an estimate of the static conductivity: it roughly depends on the product of the inverse mass and the density of electrons.

In Table 4, a diagonal element of the inverse mass averaged over the occupied states, the mean value of grad $\epsilon(n, \vec{k})^2$ over the Fermi surface and the plasma frequencies $\omega_{pl,b}$ and $\omega_{pl,f}$ are listed. A crude estimate of the dc conductivity of these compounds has been obtained by using a relaxation time τ which appropriately explains the room temperature conductivity of polycrystalline Cu, say 6.0 10^5 $(\Omega\text{cm})^{(-1)}$. The last column lists the ratio of these conductivities. From these results, we learn that asymptotic behaviour of $\Re\chi$ is dominated by the interband contribution as the intraband contribution is smaller up to one order. The effective inverse mass and the inner product of grad $\epsilon_{n,\vec{k}}$ show a stronger variation; in the compounds with Lu and Yb, the corresponding values are comparable with those of Cu, but in the compounds with Tm and Er the inner product of grad $\epsilon_{n,\vec{k}}$ is up to three order of magnitudes smaller with the consequence that in this context $ErGa_3$ turns out to be a semimetal. The close similarity of the intersections with the Fermi surface displayed in Figures 7 and 11 arouses the suspicion that the model considering the 4f electrons as part of the core will produce a dc-conductivity comparable with Cu.

In the long-wave limit, the interband contribution of the response function reduces to the sum

$$\chi_{\text{inter}}(\vec{q}, \vec{q}, \omega) = \hbar^2 \frac{q_\mu, q_\nu}{m^2} 2 \sum_{n \neq n', \vec{k}} \frac{\left\langle n, \vec{k} \middle| p_\mu \middle| n', \vec{k} \right\rangle}{\epsilon_{n,\vec{k}} - \epsilon_{n',\vec{k}}} \frac{\left\langle n', \vec{k} \middle| p_\mu \middle| n, \vec{k} \right\rangle}{\epsilon_{n',\vec{k}} - \epsilon_{n,\vec{k}}} \times \frac{f\left(\epsilon_{n,\vec{k}}\right) - f\left(\epsilon_{n',\vec{k}}\right)}{\epsilon_{n,\vec{k}} - \epsilon_{n',\vec{k}} + \hbar\omega + i\eta}, \tag{4}$$

$\langle n, \vec{k} | p_\mu | n', \vec{k} \rangle$ are the matrix elements of the Kohn-Sham Bloch functions and $\epsilon_{n,\vec{k}}$, $f(\epsilon_{n,\vec{k}})$ the corresponding eigenvalues and occupation numbers. The factor 2 in front accounts for the spin degeneracy. The sum over the wave vector $\vec{k}$ runs over the BZ whereas over n and n' extends over all Bloch states obtained in the KS scheme for a fixed value of $\vec{k}$, occupied or nonoccupied, in present case up to 240 states with energies up to 250 Ryd above the Fermi level. This requirement has often been overseen in previous investigations. As usual this expression may be decomposed in a real and in an imaginary part. By using the identity

$$\sum_{n' \neq n} \frac{\left\langle n, \vec{k} \middle| p_\mu \middle| n', \vec{k} \right\rangle \left\langle n', \vec{k} \middle| p_\nu \middle| n, \vec{k} \right\rangle}{\epsilon_{n,\vec{k}} - \epsilon_{n',\vec{k}}} = \frac{1}{2} m \delta_{\mu\nu}, \tag{5}$$

which corresponds to the Thomas-Reiche-Kuhn sum rule in atom physics [30] at large values of ω the real part of the interband contributions reduces to

$$\frac{4\pi e^2}{q^2 V_c} \Re\chi_{\text{inter}}(\vec{q}, \vec{q}, \omega) = \frac{\omega_{pl,f}^2}{\omega^2}, \tag{6}$$

in the long-wave limit. The abbreviation $\omega_{pl,f}$ is the plasma frequency of a free electron gas,

$$\omega_{pl,f}^2 = \frac{4\pi e^2}{m} \frac{2}{V_c} \sum_{n,\vec{k}} f\left(\epsilon_{n,\vec{k}}\right), \tag{7}$$

which only depends on the density of the valence electrons $(2/V_c) \sum_{n,\vec{k}} f(\epsilon_{n,\vec{k}})$. Thanks to the completeness of the Bloch functions (see (5)), all specific information for example, the

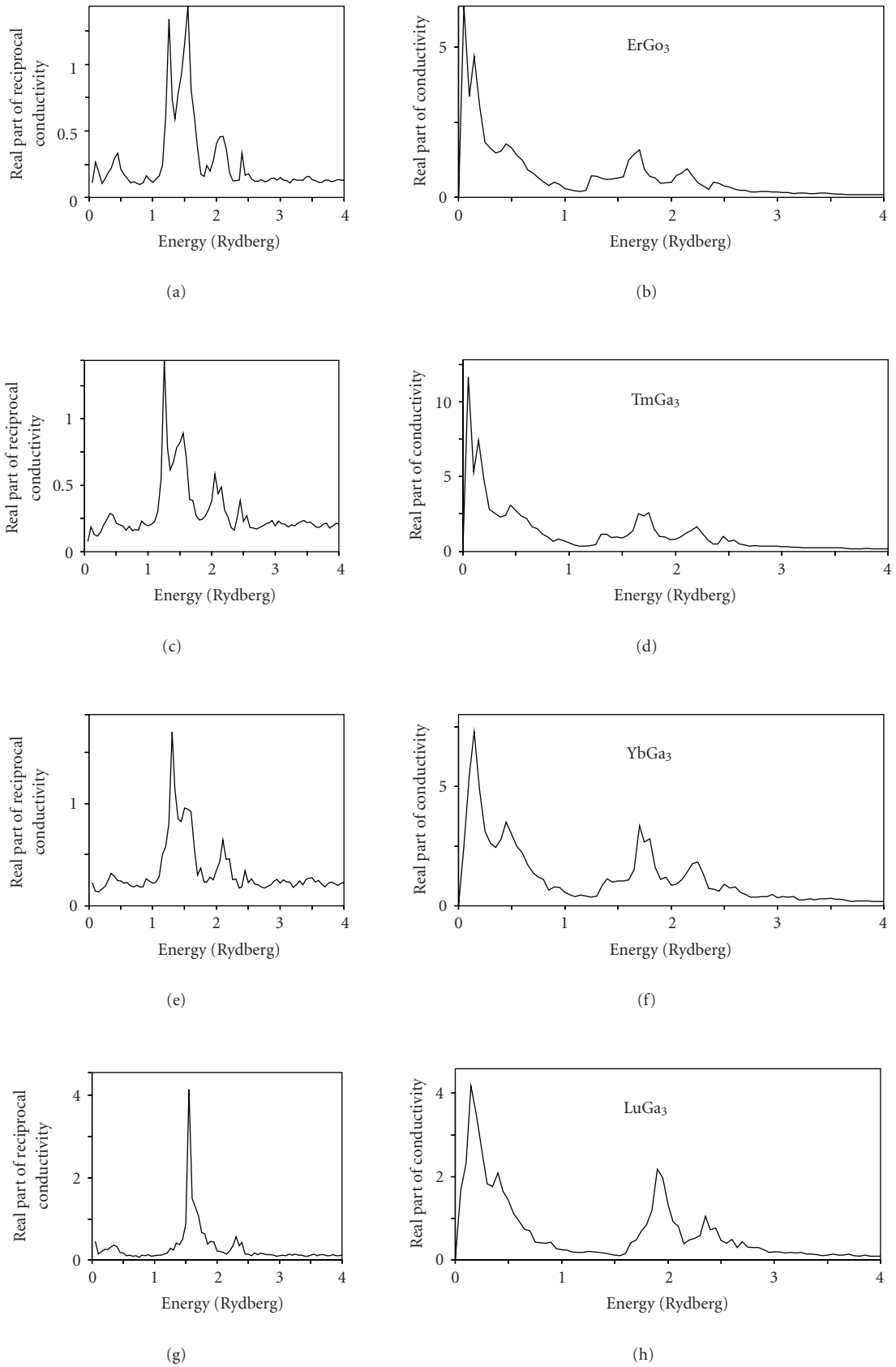

Figure 14: Frequency dependence of the real part of the conductivity (right panel) and of reciprocal conductivity (left panel) of rare-earth. Sharp spikes in the left panels indicate the possibility of collective excitations.

band structure or the matrix elements of the momentum operator has no influence on the asymptotic behaviour of the interband contributions $\Re\chi_{\text{inter}}(\vec{q},\vec{q},\omega)$ at long wavelength.

Partial integration of (2) has the result that $\chi_{\text{intra}}(0,0,\omega)$ has the same asymptotic behaviour with plasma frequencies analogously defined as in (7) with the sole difference that $1/m$ is substituted by the mean value of the tensor of the inverse mass. Both objects are only abbreviations which have nothing to do with collective excitations of the valence electrons. As consequence of the causality the infinite integral over the imaginary part at long wave length again gives the square of the free plasma frequency,

$$\frac{4\pi e^2}{q^2 V_c}\frac{1}{\pi}\int_{-\infty}^{\infty}\omega\Im\chi_{\text{inter}}(\vec{q},\vec{q},\omega)d\omega = \omega_{pl,f}^2. \tag{8}$$

It can be considered as a sum rule of a suitably defined conductivity [31].

The numerical work is largely analogous to previous investigations [32, 33]. The eigenvalues $\epsilon_{n,\vec{k}}$, their gradients, and the matrix-elements of the momentum operator $\vec{p}$ were evaluated using the MAPW results without any further approximation. As a check, the sum rule (5) was used. Figure 14 shows the frequency dependence of the conductivity $\sigma(\vec{q},\vec{q},\omega)$ in the long-wave limit in the region $0 \le \hbar\omega \le 3$ Rydberg, on the right side the real part and on the left side the real part of the reciprocal conductivity, respectively, formally defined by $\Re\sigma/((\Re\sigma)^2 + (\Im\sigma)^2)$. This expression is sensitive to collective excitations of the valence electrons similar to the energy loss function in the conventional theory.

At low values of ω, the series of compounds shows a margin difference: $ErGa_3$ and $TmGa_3$ have a structure with two well-separated peaks whereas the other two compounds have a singular peak only. Above 0.25 Ryd, the real parts of the conductivity of all four compounds look quite similar. Up to 1 Ryd, the reciprocal conductivity is without any structures. The peak structures near 1.6 Ryd, especially pronounced in $LuGa_3$, indicated the possibility of collective excitations of the valence electrons of plasmon type.

5. Summary

The electronic structure of the compounds $ReGa_3$ is found to be very sensitive to the constituent Re due to the location of the 4f bands relative to the Fermi level. In the heaviest compound, Lu, the 4f bands are quite small and far from the Fermi level E_F. The remaining valence bands have the characteristic features of an s-p-d complex and the sections of the Fermi surface with high symmetry planes of the BZ are quite similar to the results obtained for $ErGa_3$ [4, 5] and $TmGa_3$ [2] when the 4f bands are assumed to be part of the cores. With decreasing core charge these bands approach E_F and strongly interact with the other valence bands. Thus the topological structure of the Fermi surface is drastically changed and has no similarity at all with the momentum density obtained by deconvoluting the measurements of the angular correlation of the electron-positron annihilation radiation. In $ErGa_3$ and $TmGa_3$, the closeness of the 4f bands to the Fermi level produces values of $N(E_F)$ which are not realistic. GGA investigations enforce the disagreement with the experimental results.

Analogous to previous investigations, the unrealistic high value of $N(E_F)$ is avoided by considering 11 4f electron as part of the core. A detailed analysis covering the whole Brillouin zone shows that the Fermi surfaces of the compounds $ErGa_3$ and $TmGa_3$ consist of different sheets allowing a great variety of orbits in magnetic fields. One of them is multiconnected, and the usual plots showing intersections with high symmetry planes do not all describe its complex shape. Therefore, it is questionable whether the Fermi surface may be solely reconstructed from measurements. It is suspected that high-precision investigations of other compounds with a nonsimple basis will yield similar results.

With regard to the ground state properties and the response to an external scalar potential, the compounds of this series behave quite similarly up to one distinct exception: in $ErGa_3$ and $TmGa_3$, the flat 4f bands are found so close to the Fermi level that they strongly influence the shape of the Fermi surface and the inverse band mass. In DFT, both compounds are semimetals. This obvious defect is cured by use of the LDA + U scheme which shifts the 4f bands slightly below the Fermi level [20].

Acknowledgments

Dr. R. Bader, LRZ München, and Dr. H. Stöhr have critically read the paper. The generous hospitality of Professor J. van Delft and Professor U. Schollwöck is gratefully acknowledged.

References

[1] V. B. Pluzhnikov, A. Czopnik, and I. V. Svechkarev, "de Haas-van Alphen effect in $ScGa_3$, $LuGa_3$ and YIn_3 ," *Physica B*, vol. 212, no. 4, pp. 375–378, 1995.

[2] V. B. Pluzhnikov, A. Czopnik, G. E. Grechnev, N. V. Savchenko, and W. Suski, "Band structure and Fermi surface of $TmGa_3$," *Physical Review B*, vol. 59, no. 12, pp. 7893–7900, 1999.

[3] A. G. Petukhov, W. R. L. Lambrecht, and B. Segall, "Electronic structure of rare-earth pnictides," *Physical Review B*, vol. 53, no. 8, pp. 4324–4329, 1996.

[4] V. B. Pluzhnikov, A. Czopnik, and G. E. Grechnev, "The Fermi surface of $ErGa_3$," *Journal of Physics Condensed Matter*, vol. 11, no. 23, pp. 4507–4516, 1999.

[5] M. Biasini, G. Ferro, G. Kontrym-Sznajd, and A. Czopnik, "Fermi surface nesting and magnetic structure of $ErGa_3$," *Physical Review B*, vol. 66, no. 7, Article ID 075126, pp. 751261–751268, 2002.

[6] G. Kontrym-Sznajd, M. Samsel-Czekała, G. E. Grechnev, and H. Sormann, "Fermi surface of $ErGa_3$," *Physica Status Solidi C*, vol. 4, no. 10, pp. 3879–3882, 2007.

[7] H. Bross, G. Bohn, G. Meister, W. Schubö, and H. Stöhr, "New version of the modified augmented-plane-wave method," *Physical Review B*, vol. 2, no. 8, pp. 3098–3103, 1970.

[8] H. Reinisch and H. Bross, "Relativistic density functional calculation of the total energy and Fermi surface of gold," *Zeitschrift für Physik B*, vol. 95, no. 2, pp. 145–150, 1994.

[9] V. Theileis and H. Bross, "Relativistic modified augmented plane wave method and its application to the electronic structure of gold and platinum," *Physical Review B*, vol. 62, no. 20, pp. 13338–13346, 2000.

[10] S. H. Vosko, L. Wilk, and M. Nusair, "Accurate spin-dependent electron liquid correlation energies for local spin-density calculations—a critical analysis," *Canadian Journal of Physics*, vol. 58, no. 8, pp. 1200–1211, 1980.

[11] J. P. Perdew, J. A. Chevary, S. H. Vosko et al., "Atoms, molecules, solids, and surfaces: applications of the generalized gradient approximation for exchange and correlation," *Physical Review B*, vol. 46, no. 11, pp. 6671–6687, 1992.

[12] J. P. Perdew, K. Burke, and M. Ernzerhof, "Generalized gradient approximation made simple," *Physical Review Letters*, vol. 77, no. 18, pp. 3865–3868, 1996.

[13] J. P. Perdew, "Density-functional approximation for the correlation energy of the inhomogeneous electron gas," *Physical Review B*, vol. 33, no. 12, pp. 8822–8824, 1986.

[14] J. P. Perdew, "Erratum: density-functional approximation for the correlation energy of the inhomogeneous electron gas," *Physical Review B*, vol. 34, no. 10, p. 7406, 1986.

[15] H. Bross, "The local density approximation limit of the momentum density and the Compton profiles of Al," *Journal of Physics Condensed Matter*, vol. 16, no. 41, pp. 7363–7378, 2004.

[16] H. Bross and R. Eder, "Self-consistent MAPW calculation with a warped muffin-tin potential. I. The electronic structure of Al and its pressure dependence," *Physica Status Solidi B*, vol. 144, no. 1, pp. 175–193, 1987.

[17] H. Bross and R. Stryczek, "Self-consistent MAPW calculation with a warped muffin-tin potential. II. The electronic structure of Li and its pressure dependence," *Physica Status Solidi B*, vol. 144, no. 2, pp. 675–692, 1987.

[18] H. Jones, *The Theory of Brillouin Zones and Electronic States in Crystals*, North-Holland, Amsterdam, The Netherlands, 1962.

[19] I. M. Lifshitz and A. M. Kosevich, "Quantum Theory of the Electrical Conductivity of Metals in a Magnetic Field," *Journal of Experimental and Theoretical Physics*, vol. 2, p. 636, 1956.

[20] to be published.

[21] V. I. Anisimov, F. Aryasetiawan, and A. I. Lichtenstein, "First-principles calculations of the electronic structure and spectra of strongly correlated systems: the LDA + U method," *Journal of Physics Condensed Matter*, vol. 9, no. 4, pp. 767–808, 1997.

[22] A. I. Liechtenstein, V. I. Anisimov, and J. Zaanen, "Density-functional theory and strong interactions: orbital ordering in Mott-Hubbard insulators," *Physical Review B*, vol. 52, no. 8, pp. R5467–R5470, 1995.

[23] A. B. Shick, A. I. Liechtenstein, and W. E. Pickett, "Implementation of the LDA+U method using the full-potential linearized augmented plane-wave basis," *Physical Review B*, vol. 60, no. 15, pp. 10763–10769, 1999.

[24] E. K. U. Gross and W. Kohn, "Local density-functional theory of frequency-dependent linear response," *Physical Review Letters*, vol. 55, no. 26, pp. 2850–2852, 1985.

[25] E. K. U. Gross, "Erratum: local density-functional theory of frequency-dependent linear response," *Physical Review Letters*, vol. 57, no. 7, p. 923, 1986.

[26] E. K. U. Gross and W. Kohn, "Density Functional Theory of Many-FermionSystems," in *Advances in Quantum Chemistry*, S. B. Trickey, Ed., vol. 21, p. 255, Academic Press, San Diego, Calif, USA, 1990.

[27] E. K. U. Gross, J. F. Dobson, and M. Petersilka, "Density-functional theory of time-dependent phenomena," in *Topics in Current Chemistry*, R. F. Nalewajski, Ed., vol. 181, pp. 81–172, Springer, Berlin, Germany, month 1996.

[28] M. Kohler, "Behandlung von Nichtgleichgewichtsvorgängen mit Hilfe eines Extremalprinzips," *Zeitschrift für Physik*, vol. 124, no. 7-12, pp. 772–789, 1948.

[29] J. M. Ziman, "Electrons," in *The Physics of Metals*, J. M. Ziman, Ed., chapter 5, Cambridge University Press, Cambridge, UK, 1969.

[30] W. Thomas, "Über die Zahl der Dispersionselektronen, die einem stationären Zustande zugeordnet sind. (Vorläufige Mitteilung)," *Die Naturwissenschaften*, vol. 13, no. 28, p. 627, 1925.

[31] D. Pines and P. Nozieres, "Normal Fermi Liquids," *The Theory of Quantum Liquids*, vol. 1, W. A. Benjamin, Menlo Park, Calif, USA, 1966.

[32] H. Bross, O. Belhachemi, B. Mekki, and A. Seoud, "Local field corrections and the influence of exchange and correlation on the microscopic longitudinal dielectric function of copper," *Journal of Physics*, vol. 2, no. 17, pp. 3919–3939, 1990.

[33] H. Bross and M. Ehrensperger, "Calculation of the Dielectric Function of Li Metals," *Zeitschrift für Physik*, vol. 97, p. 17, 1995.

[34] P. T. Landsberg, "Simple Perturbation Methods in Band Theory," in *Solid State Theory*, P. T. Landsberg, Ed., chapter B17, Wiley-Interscience, London, UK, 1969.